Remote Sensing of Environment 321 (2025) 114688

Contents lists available at ScienceDirect

Remote Sensing of Environment

journal homepage: www.elsevier.com/locate/rse

Sediment accumulation at the Amazon coast observed by satellite gravimetry

Earthu H. Oh [a], Ki-Weon Seo [a,*], Taehwan Jeon [b], Jooyoung Eom [c], Jianli Chen [d,e,f], Clark R. Wilson [g,h]

[a] Department of Earth Science Education, Seoul National University, Seoul, Republic of Korea
[b] Center for Educational Research, Seoul National University, Seoul, Republic of Korea
[c] Department of Earth Science Education, Kyungpook National University, Daegu, Republic of Korea
[d] Department of Land Surveying and Geo-informatics, Hong Kong Polytechnic University, Hong Kong, China
[e] Research Institute for Land and Space, The Hong Kong Polytechnic University, Hong Kong, China
[f] The Hong Kong Polytechnic University Shenzhen Research Institute, Shenzhen, China
[g] Department of Earth and Planetary Sciences, Jackson School of Geosciences, University of Texas at Austin, Austin, TX, USA
[h] Center for Space Research, University of Texas at Austin, Austin, TX, USA

ARTICLE INFO

Editor: Menghua Wang

Keywords:
Satellite gravimetry
Coastal geodesy
Amazon River
Sediment transport

ABSTRACT

Terrestrial sediment transport through large rivers exerts a significant impact on coastal morphology, marine ecosystems, and human livelihoods. Accurately measuring these sediment discharges has long been a challenge. Traditional in-situ methods fall short of providing comprehensive and continuous assessments of sediment dynamics due to spatiotemporal and economic constraints. While remote sensing techniques using satellite imagery have offered valuable insights into sediment transportation and deposition, their scope is primarily restricted to observing suspended sediment loads rather than total loads. Sediment accumulation at river margins will cause gravity increases observable by the Gravity Recovery and Climate Experiment (GRACE) and GRACE Follow-On (GFO) missions. Previous efforts to observe sediment signals lacked proper corrections for various GRACE/GFO issues, including leakage of signals from surrounding land, variations in nearby ocean mass, and noise levels that typically exceed sediment signal magnitudes. In this study, we develop a new approach to obtain a satellite gravity estimate of sediment accumulation along the Amazon coast where the largest amount of sediment deposition is expected. We address limitations in previous studies using three steps: Forward modeling to suppress leakage of signal from land to oceans; adjusting ocean mass change via the sea level equation; and filtering using empirical orthogonal functions. The estimated accumulation rate of sediment on the Amazon continental shelf is approximately 1301 Mtons per year for the period June 2002 to May 2023. This estimate is slightly higher than the results from field-based studies, which fall in the range 550 to 1030 Mtons per year.

1. Introduction

Coastal areas are dynamic zones of mass exchange, characterized by complex interactions across diverse temporal and spatial scales. This variability is especially evident near river mouths, where freshwater and sediments are transported from land to oceans. As sedimentation rates in these regions significantly alter their surrounding environments, precise measurement is crucial for enhancing our understanding of surface processes and landscape dynamics. Improved monitoring of sediment transport provides valuable insights into its impact on coastal morphology, ecological systems, and sedimentary processes.

Total sediment discharge from rivers in lower latitudes was estimated to be approximately 20 Gtons/yr (Milliman and Syvitski, 1992). Table 1 summarizes a number of studies for the 10 largest rivers, many completed in the pre-GRACE (Gravity Recovery and Climate Experiment) era. Most studies have used in-situ data, such as measurements from sediment gauges, acoustic backscattering, seismic profiles, and piston coring (Armijos et al., 2017; de Oliveira et al., 2021; Simpson and Oltmann, 1993; Alexander Jr et al., 1986; Kuehl et al., 1982). Such data are sparse in both space and time, motivating the use of satellite observations. For example, Martinez et al. (2009) quantified the annual discharge of Amazon River sediments from the Moderate Resolution

* Corresponding author.
E-mail address: seokiweon@snu.ac.kr (K.-W. Seo).

https://doi.org/10.1016/j.rse.2025.114688
Received 16 October 2024; Received in revised form 20 February 2025; Accepted 24 February 2025
Available online 5 March 2025

Table 1
Estimated sedimentation rate for the 10 largest rivers in the world, many in the pre-GRACE era.

River		Area $\times 10^6 km^2$	Average Sediment Load $\times 10^9 kg\ (Mtons)/yr$	Data Base
1	Amazon	6.1	1200	Meade et al., 1985
2	Ganges-Brahmaputra	1.59	1060	Hossain data (unpub.)
3	Irrawaddy	0.43	260	Milliman and Meade, 1983
4	Magdalena	0.24	220	Milliman and Meade, 1983
5	Mississippi	3.3	210	Meade et al., 1990
6	Godavari	0.31	170	Biksham and Subramanian, 1988
7	Yangtz	1.9	154	Wang et al., 2011
8	Huanghe (Yellow)	0.77	150	Wang et al., 2006 and 2007
9	Orinoco	0.99	150	Meade pers. comm.
10	Mekong	0.79	160	Milliman and Meade, 1983

Imaging Spectroradiometer (MODIS) reflectance calibrated by field data. Satellite measurements from optical imagery provide estimates of suspended sediment loads, but total discharge is not well constrained.

GRACE and GRACE Follow-On (GFO) observations provide direct measures of near-surface mass change. Here we develop an approach to use these data to estimate changes in continental shelf sediment mass. Since the launch of GRACE in March 2002, GRACE and GFO have played a pivotal role in examining various mass change signals, including ice mass loss, sea level rise, groundwater depletion, drought and flood events, and solid Earth deformation (Tapley et al., 2019; Chen et al., 2022). Recent studies have attempted to identify GRACE/GFO signals associated with sediment transport and deposition associated with large rivers (Mouyen et al., 2018; Chang et al., 2019). However, the relatively small spatial scales and magnitudes of sediment signals require that other gravity change signals must first be removed. Limited spatial resolution (~300-400 km) of GRACE/GFO data leads to spatial leakage so that coastal zone/continental shelf signals are a mixture of signals from nearby sources. In coastal areas the largest contamination is likely from water mass change over both land and oceans. Additional contamination comes from GRACE/GFO noise.

Previous GRACE/GFO sedimentation studies attempted to correct for problems outlined in the previous paragraph. Mouyen et al. (2018) obtained GRACE estimates of sediment discharge from 13 large rivers, and compared these with in-situ data. Hydrological model data were used to correct for spatial leakage from adjacent land, but no corrections were made for ocean mass increase that would be primarily due to terrestrial ice melting. Chang et al. (2019) estimated sediment discharge of the Yangtze River into the East China Sea, using a forward-modeling land leakage correction, and a regional ocean mass correction using satellite altimetry and steric (volume expansion) data.

In this study, we develop an estimate for the Amazon based upon GRACE/GFO satellite gravity data. Because seasonal variations are probably not well resolved by GRACE/GFO (e.g., Mouyen et al., 2018), we focus on estimating the long-term sediment accumulation rate. Table 1 shows that both the Amazon and Ganges-Brahmaputra signals are large in magnitude and probably more detectable using GRACE/GFO relative to other rivers. But the Amazon has certain advantages: (1) no significant solid Earth change processes are nearby, such as tectonic activity and Glacial Isostatic Adjustment (GIA), and (2) the deposition site is known to be relatively near the river mouth (Nittrouer et al., 1995), creating a spatial pattern distinct from other mass change contributions. In contrast, the Ganges-Brahmaputra River deposits sediment over a broad area due to regional ocean dynamics and the complexity of river channels along the coast (Paszkowski et al., 2021), and there are co- and post-seismic signals from nearby subduction zone earthquakes (Chen et al., 2007; Han et al., 2006; Han et al., 2015).

Section 3 explains how water mass changes on both land and oceans

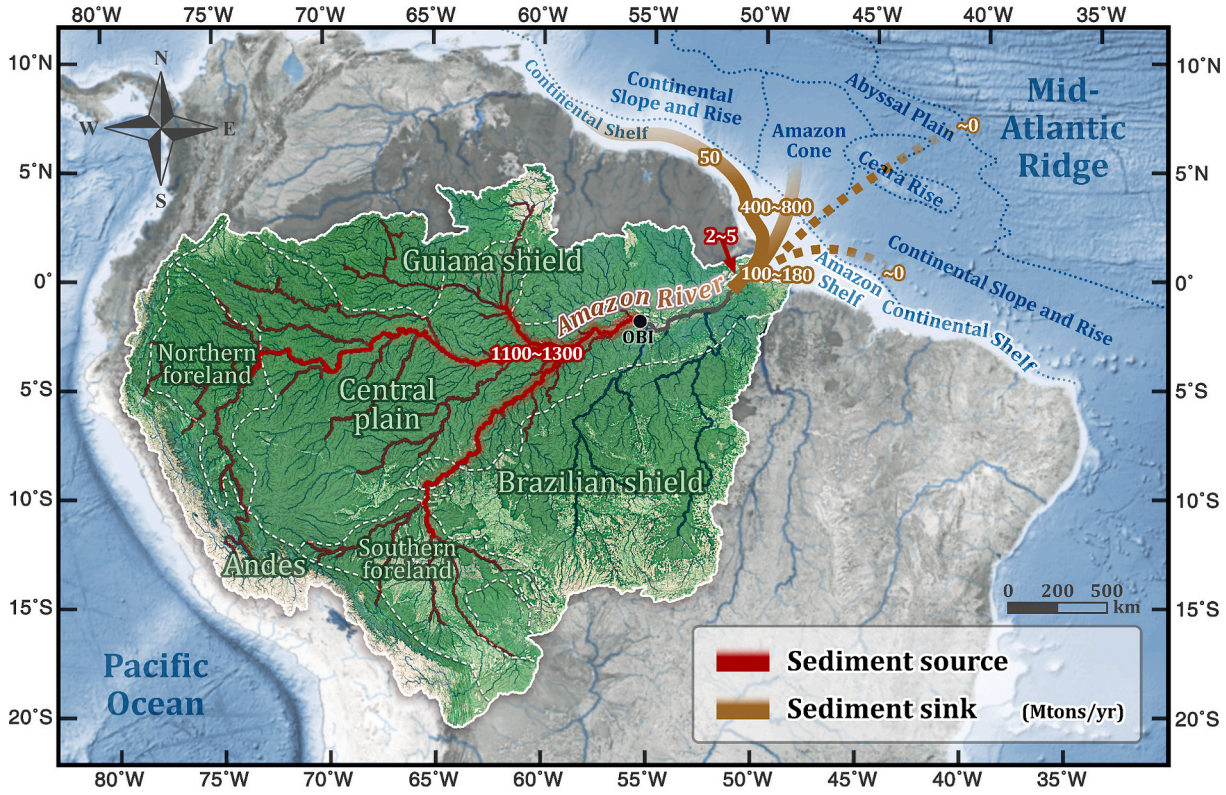

Fig. 1. The geomorphological domain of the Amazon basin with the sediment routing system. (OBI: Óbidos station, data collection from Nittrouer et al., 1995).

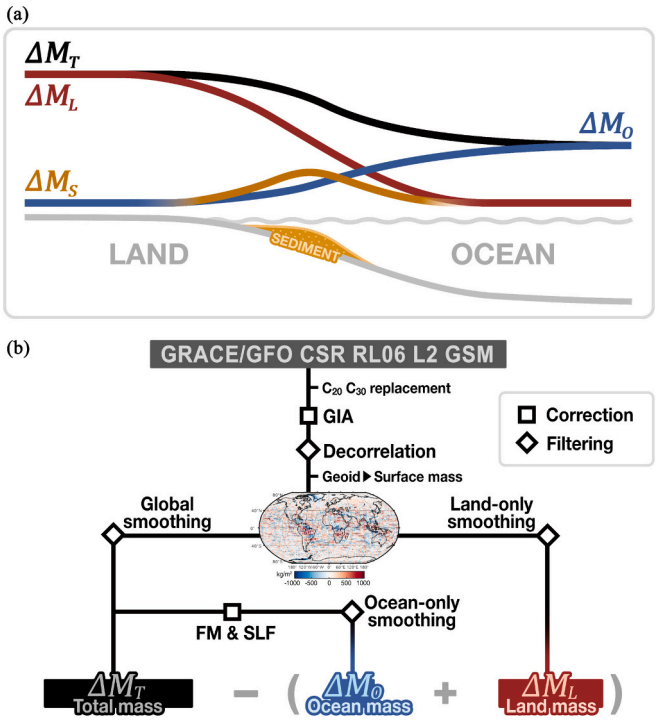

Fig. 2. (a) Schematic illustration of mass contributors near the Amazon coast and (b) flowchart of GRACE/GFO data processing. (FM: forward modeling, SLF: sea level filter-resulting from applying the sea level equation).

were estimated from GRACE/GFO data. After removing these, the sediment discharge signal should remain plus noise. We applied empirical orthogonal function (EOF) analysis for signal separation. Filtered signals using cyclostationary EOF (CSEOF) and rotated EOF (REOF) techniques provide estimates of sedimentation rate in close agreement with estimates from in-situ data.

2. Amazon regional geography

The Amazon basin is the world's most extensive drainage system, with an area of about 5,900,000 km^2 (Callede et al., 2010), over latitude 5°N to 20°S and longitude 80°W to 50°W. Fig. 1 illustrates topographic and sedimentary features, including three main geomorphological components and their areal extent: the Andes (25 %), Guiana and Brazilian Shields (51 %), and the Central Plain (24 %). The Andes, in the west, feature an active orogenic zone and two foreland basins, and serve as the primary sediment source. The Guiana and Northern and Southern Brazilian Shields are a secondary sediment source. In the center of the Amazon basin, the Central Plain is a large sedimentary basin channelized by the Amazon River and its tributaries, transporting sediments from the Andes and the shields (Moquet et al., 2016).

The Amazon River channel annually discharges around 2.3 to 3.1 Gtons of sediments along with 6.5 to 6.6 $\times$ 10^{12} m^3 of water mass from the highlands (Dai and Trenberth, 2002; Callede et al., 2010). However, only 1.1 to 1.3 Gtons pass through the Óbidos station in the lower Amazon River, with the rest dispersed across floodplains and levees of the central plain (Aalto et al., 2006; Rudorff et al., 2014; Nittrouer et al., 2021). A portion, approximately 550–1030 Mtons, passing through the Óbidos station, arrives at the river margin and is deposited offshore (Nittrouer et al., 1995). The sediment discharge of the Amazon River shows annual variations, increasing during a wet season from March to August and decreasing during a dry season from September to February (Moquet et al., 2016). A previous study estimated the peak-to-peak annual variation below 0.1 Gtons (Mouyen et al., 2018). This would be difficult to observe with GRACE/GFO, so our focus is on estimating a sediment-related linear trend over about two decades.

3. Data and methods

3.1. GRACE/GFO level-2 processing

We used GRACE/GFO RL06 level-2 solutions from the Center for Space Research (CSR), from June 2002 to May 2023. Data are absent from June 2017 to May 2018 between GRACE and GFO missions. The RL06 level-2 solutions are provided as fully normalized gravity spherical harmonic (SH) coefficients up to degree and order 96. As in previous GRACE/GFO studies, we replaced degree-2 order-0 (ΔC_{20}) and degree-3 and order-0 (ΔC_{30}) coefficients with Satellite Laser Ranging (SLR) values (Loomis et al., 2019), and removed GIA using the ICE6G-D model (Peltier and Argus, 2018). GRACE/GFO longitudinal stripe noise was reduced using a combination of a decorrelation filter and a 400 km Gaussian smoothing filter (Swenson and Wahr, 2002; Swenson and Wahr, 2006). The decorrelation filter fits spurious patterns of SH even or odd coefficients at a given degree using polynomials and removes them. The Gaussian filter is designed to suppress spatially high-frequency features in GRACE/GFO data (Wahr et al., 1998). By averaging values at each spatial point with those of its neighbors within a specified radius (in this case, 400 km), this filter effectively passes larger-scale signals in the GRACE data. A 300–400 km averaging radius is commonly used in GRACE/GFO studies. These filtering steps lower GRACE/GFO spatial resolution and increase spatial leakage, so the surface mass change estimates (in kg/m^2 unit) are a combination of smoothed signals from various sources (Wahr et al., 1998). We denote smoothed GRACE/GFO surface mass change as ΔM_T.

3.2. Mass change sources contributing to ΔM_T

Terrestrial surface mass change signals (denoted as ΔM_L) are present in ΔM_T due to spatial signal leakage in coastal regions. ΔM_L is mostly associated with water mass variations within the adjacent Amazon basin. Ocean mass variation (ΔM_O) also contributes. It is governed by gravitational attraction, surface load deformation, and ocean mass changes from regional and global sources. After correcting both water-related contributions (ΔM_L and ΔM_O) from ΔM_T, the residual should include the sediment accumulation signal (ΔM_S), the object of this study. Hence, we decompose the GRACE-derived mass changes ΔM_T at the Amazon River continental margin as:

$$\Delta M_T = \Delta M_L + \Delta M_O + \Delta X. \quad (1)$$

where ΔX represents the residual signals of ΔM_T after correcting the water-related signals of ΔM_L and ΔM_O. ΔX is the sum of our target signal ΔM_S and noise Δe:

$$\Delta X = \Delta M_S + \Delta e. \quad (2)$$

Δe may arise from GRACE/GFO error (e.g., residual longitudinal stripe noise), errors in geophysical models used in GRACE/GFO data processing, and errors in ΔM_L and ΔM_O (estimates).

All contributions in Eq. (1) have spatial scales associated with the filtering used to obtain ΔM_T. ΔM_L is expected to be the largest contaminating source in the coastal region. When using globally smoothed solutions such as ΔM_T, it is difficult to separate relatively small signals like ΔM_S from the likely stronger leakage ΔM_L. We used GRACE/GFO signals over land before and after Gaussian smoothing to estimate ΔM_L. Prior to the final step of Gaussian smoothing, there is evidence of residual longitudinal stripe noise (implying imperfection of the decorrelation filter), but spatial leakage is less evident. Then we apply 400 km Gaussian smoothing to estimate ΔM_L as that signal which is now located offshore. This should provide a reasonable estimate of leakage into the oceans from ΔM_T, with perhaps some error. The residual leakage in ΔM_L might still be an important source of uncertainty

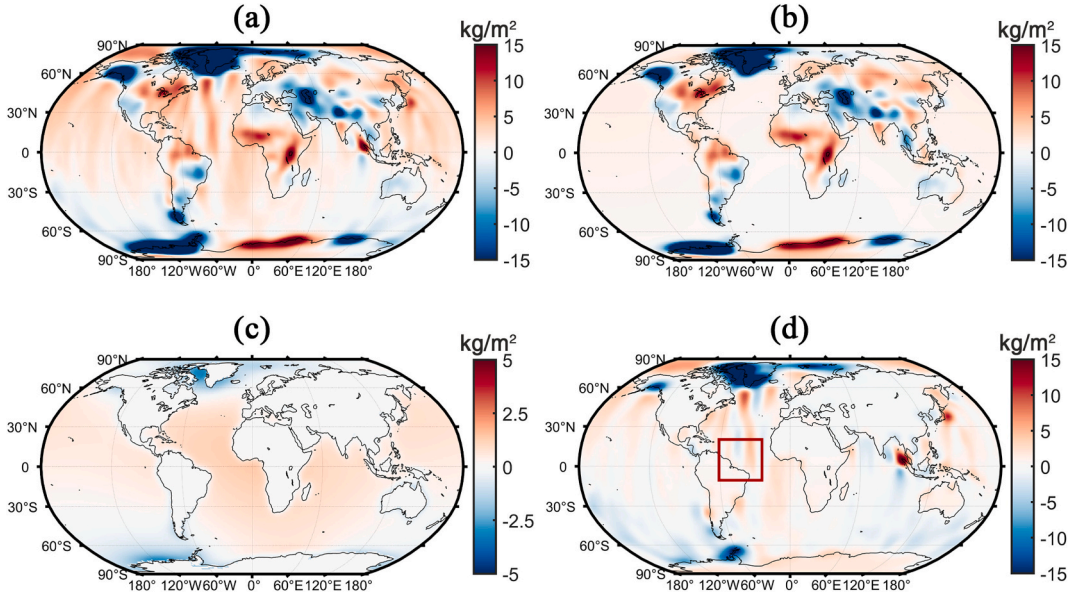

Fig. 3. Global trend maps of mass change estimates over a 21-year period (June 2002 – May 2023). The figures show trend maps for the following variables: (a) ΔM_T, total mass changes; (b) ΔM_L, land mass changes; (c) ΔM_O, ocean mass changes; and (d) ΔX representing $\Delta M_T - \Delta M_L - \Delta M_O$. The red box that covers latitudes 20°N to 10°S and longitudes 60°W to 25°W shows our study area. (For interpretation of the references to colour in this figure legend, the reader is referred to the web version of this article.)

in sedimentation studies at river margins using GRACE/GFO, and would contribute to Δe. However residual leakage will be correlated with temporal and spatial variability of terrestrial water storage change in adjacent areas and should have a spatial pattern that differs from the sedimentation signal. As a result, the residual leakage can be separated via EOF analysis and filtering as detailed in Section 3.3 below.

An additional, and possibly important, contributor to Δe may be uncorrected residual effects of ocean dynamics and tides (Han et al., 2004; Shihora et al., 2022). In the monthly samples of GRACE/GFO data, the effects of ocean tides and ocean bottom pressure, including barometric pressure, are corrected using models. However, residual effects of ocean dynamics and tides may remain in ΔM_T. These residuals can be also effectively identified and separated using EOF analysis and filtering.

Previous studies estimated ΔM_S from GRACE data after correction of ΔM_L and ΔM_O by using hydrological models (Mouyen et al., 2018) and satellite altimetry data after correction for steric effects (Chang et al., 2019), respectively. In this study, we directly estimated ΔM_L and ΔM_O from GRACE/GFO data to enhance the accuracy of the estimation. We estimated ΔM_O using global forward modeling (FM) (Chen et al., 2013) to find total water mass change over land, and then distributed the negative of this quantity over the oceans using the sea level equation (SLE) (Farrell and Clark, 1976). FM finds water and ice mass changes over land by suppressing signal leakage into the oceans. The algorithm iteratively smooths and updates mass changes over land until the solution converges to a land-only ΔM_T. Each iteration update is the difference between successive smoothed solutions.

The SLE creates spatially-variable ocean mass changes (whose total is the negative of ΔM_T) by requiring that the sea surface conforms to a changed geoid. Land mass change may arise from both water/ice and sedimentation, so estimated ocean mass changes using the SLE ought to include a sediment effect. However, considering the total amount of sedimentation in Table 1, the contribution to sea level change would be about 0.01 mm/yr, negligible compared to water and ice mass contributions to sea level rise, about 2.07 mm/yr (Kim et al., 2019). Consequently, it is reasonable to use the SLE considering only terrestrial water and ice mass changes. Estimates using this method have been found to be consistent with other sea level change observations, such as altimetry and steric sea level changes (Jeon et al., 2021).

The final estimate of ΔM_O is found by applying 400 km Gaussian smoothing to the ocean mass change estimate. Fig. 2(a) and 2(b) illustrate schematically ΔM_T at the Amazon River outlet and GRACE/GFO data reduction flow charts, respectively.

Fig. 3 shows mass trend maps of ΔM_T, ΔM_L, ΔM_O, and ΔX during the entire period June 2002 to May 2023. Fig. 3(a) shows the trend of ΔM_T, long-term surface mass changes from ordinary post-processing of GRACE data. The Amazon coast shows an increase in mass, likely to be signal leaking from water mass increasing within the Amazon basin. The trend of ΔM_L estimates, the difference between smoothed and unsmoothed GRACE/GFO data, is shown in Fig. 3(b). The FM algorithm and SLE computation provide the ΔM_O estimates, and their trend map is shown in Fig. 3(c). All values used in subpanels 3(a) to 3(c) were smoothed using a 400 km Gaussian filter.

After computing and subtracting ΔM_L and ΔM_O, we obtain residual changes ΔX, the trend map of which is shown in Fig. 3(d). ΔX may contain various errors Δe. For example, in some regions, there will be earthquake-related signals (e.g., associated with large events near Sumatra and Japan) and GIA model errors (likely evident around the Antarctic Peninsula), but these are not likely to be important near the Amazon. Longitudinal stripe noise is evident over much of the globe and also the Amazon coast, which is likely due to the combined effect of the GRACE/GFO orbit configuration and errors in ocean dynamic and atmospheric pressure models used in GRACE/GFO processing. Further temporal-spatial filtering using EOF methods is required to suppress errors in ΔX.

3.3. Estimation of the sedimentation signal via EOF methods

Subtracting ΔM_L and ΔM_O monthly estimates from ΔM_T results in ΔX from June 2002 to May 2023. ΔX is evaluated on a $1° \times 1°$ grid within the red box shown in Fig. 3(d), from 20°N to 10°S latitude and 60°W to 25°W longitude, which covers 31×36 grid points. Prior to EOF filtering, we excluded values that fell outside three standard deviations (3σ) of the time series at each grid point and linearly interpolated values from adjacent months to replace them. Residual land leakage contaminating ΔX is likely dominted by seasonal variability, so we then subtracted seasonal sinusoids from each grid value in ΔX. A total of 240 monthly samples is available at each grid point, creating a space-time dataset

with a gap between GRACE and GFO missions.

EOF methods are widely used for decomposing space-time data to find underlying spatial and temporal characteristics (Navarra and Simoncini, 2010). A diverse range of techniques based on EOF concepts has been developed. Here, we sequentially applied CSEOF and REOF methods on ΔX to separate signal (ΔM_S) from errors (Δe). As mentioned earlier, ΔX may still contain errors correlated with temporal and spatial variability of other geophysical sources, which persist despite previous data processing.

To remove these errors that do not share the geophysical processes of ΔM_S, we first applied the CSEOF method to ΔX (Kim et al., 2015). In the context of our GRACE data corrections, we hypothesize that Δe primarily shows spatially correlated patterns with greater temporal variations than seasonal changes. In contrast, ΔM_S is anticipated to display a stable spatial configuration, either remaining constant or evolving gradually over time (Eom et al., 2017a, 2017b). To effectively differentiate between these patterns, we employ the CSEOF method, which is specifically designed to identify temporally evolving spatial patterns in geophysical processes (Kim, 2017). For the CSEOF decomposition for our space-time dataset $\Delta X(x,t)$, we first consider the standard form of EOF decomposition:

$$\Delta X(x,t) = \sum\nolimits_l E_l(x) Z_l(t) \tag{3}$$

where x and t denote grid position and time step, respectively. The subscript l is the mode index. $E_l(x)$ represents the spatial pattern or loading vector for the l-th mode. The set of $E_l(x)$ comprises eigenfunctions derived from the covariance of $\Delta X(x,t)$. The temporal variation of each mode is described by principal component, $Z_l(t)$. According to the nature of an *eigenproblem*, the E_ls are orthogonal to each other, and the corresponding Z_ls are also uncorrelated with each other.

The conventional EOF decomposition assumes stationarity of $\Delta X(x,t)$, hence that its covariance is time independent. Space-time dependence in geophysical data, therefore, can be better understood using CSEOF which considers periodic (i.e., cyclostationarity) data. CSEOF decomposes $\Delta X(x,t)$ as follows:

$$\Delta X(x,t) = \sum\nolimits_n E_n^c(x,t) Z_n^c(t) \tag{4}$$

where subscript n is the CSEOF mode index and $E_n^c(x,t)$ represents the cyclostationary loading vectors (CSLV) with periodic evolution with a nested period of d, that is, $E_n^c(x,t) = E_n^c(x,t+d)$. $Z_n^c(t)$ is the corresponding time series of each principal component (PC). Considering the dominant periodicity of Earth system, we selected a nested period d to be 12 months as in many previous studies (Kim et al., 2020; Kim et al., 2015; Hamlington et al., 2011). Therefore, CSEOF decomposition at each mode represents the spatial and temporal evolution over 12 months, with amplitudes modulated by Z_n^c throughout the entire study period (June 2002 to May 2023).

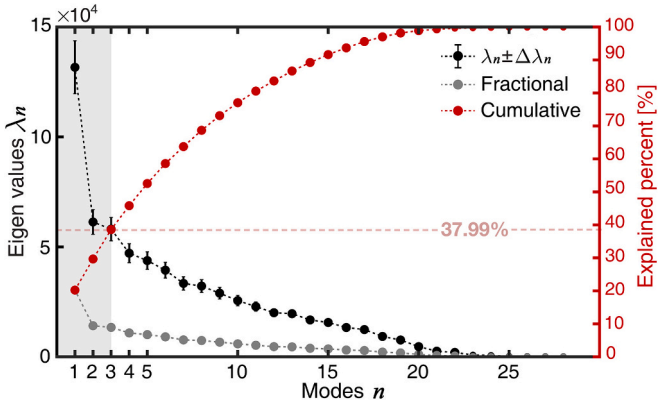

Fig. 4. Eigenvalues (λ_n) of each CSEOF mode with confidence limit ($\Delta\lambda_n$). The proportions of the total variance explained by fractional (gray curve with dots) or cumulative eigenvalues (red curve with dots) are additionally provided. (For interpretation of the references to colour in this figure legend, the reader is referred to the web version of this article.)

A detailed explanation for computing CSLV and PC can be found in Kim and North (1997). Here we briefly review procedures for the CSEOF decomposition. Due to the computational cost of handling space-time dependent covariance, applying $E_l(x)$ and $Z_l(t)$ from the standard EOF is practically useful in the CSEOF decomposition. For the preparatory steps, we first selected the 94 leading modes of the EOF accounting for more 99.9 % of the variance of ΔX, and computed the local Fourier coefficients of $Z_l(t)$, $a_{l,k}(t)$, using a windowed spectral analysis (Gardner, 1994; Kim and North, 1997):

$$a_{l,k}(t) = \int_{-\infty}^{\infty} w(t-\tau) Z_l(\tau) exp\left(-\frac{2\pi i k \tau}{d}\right) d\tau \tag{5}$$

where $w(t)$ is the spectral window defined as $sin(\pi t/d)/\pi t$. As discussed above, d is set to 12, representing one calendar year. The frequency parameter, k, is an integer with a maximum value of $d/2$ determined based on the Nyquist frequency for our monthly data. $Z_l(t)$ can be directly applied for the CSEOF, but Fourier analysis is suitable for obtaining the periodicity of the data and is additionally useful for reducing computational cost.

Similar to $E_l(x)$ in Eq. (3), $E_n^c(x,t)$ in Eq. (4) is obtained by solving an eigenproblem for the space-time covariance of $\Delta X(x,t)$ considering the nested period of d. The size of this covariance kernel is, therefore, d squared times larger than that of the standard EOF case, requiring substantial computational resources. Instead of dealing with such a large kernel, we can efficiently conduct the same CSEOF analysis in both EOF space and in the spectral domain (Kim et al., 1996; Kim and North, 1997). Through the preparatory data processing, we constructed a much smaller kernel using 7 sets of the local Fourier coefficients ($a_{l,k}(t)$) for each 94 Z_ls. Using the space-time covariance constructed by $a_{l,k}(t)$, an eigenvector $b_n(l,k)$ at a given frequency parameter, k, for the l-th EOF mode can be obtained. Therefore, CSLVs for n-th mode in Eq. (4) are given as follow:

$$E_n^c(x,M) = \sum\nolimits_l E_l(x) \sum_k b_n(l,k) exp\left(\frac{2\pi i k}{d} M\right) \tag{6}$$

where M is a monthly index in a canlendar year. Similarly, PC time series for n-th mode can be obtained as:

$$Z_n^c(t) = \sum\nolimits_l \sum\nolimits_k b_n(l,k) a_{l,k}(t). \tag{7}$$

The decomposition of ΔX using Eq. (4) provides the set of CSEOF modes, and ΔM_S contributions are likely included within a few leading modes. We selected those CSEOF modes for ΔM_S based on the confidence limit of each mode. The confidence interval $\Delta\lambda_n$ of an EOF mode is defined by (North et al., 1982):

$$\Delta\lambda_n = \lambda_n \sqrt{2/N^*} \tag{8}$$

where λ_n represents the eigenvalue of the n-th mode, and N^* is the number of degrees of freedom, equal to the total number of temporal samplings minus one. The $\Delta\lambda_n$ values usually have distinct intervals when the mode is well decomposed. Using λ_n and $\Delta\lambda_n$, we selected a few leading CSEOF modes as the filtered data set, $\Delta X'$.

The reconstructed field, $\Delta X'$, obtained from the CSEOF may still contain residual noise. The ΔM_S contribution is expected to exhibit a distinct spatial distribution near the river mouth, unlike Δe. To isolate a single mode confined to the coastal area, we additionally employed the REOF method, allowing us to separate residual errors from $\Delta X'$ (Richman, 1986; Hannachi et al., 2007). Since this technique utilizes the spatial modes decomposed by the conventional EOF, we applied Eq. (3) to $\Delta X'$ again and selected the first two modes for $\Delta X''$. Two modes used in

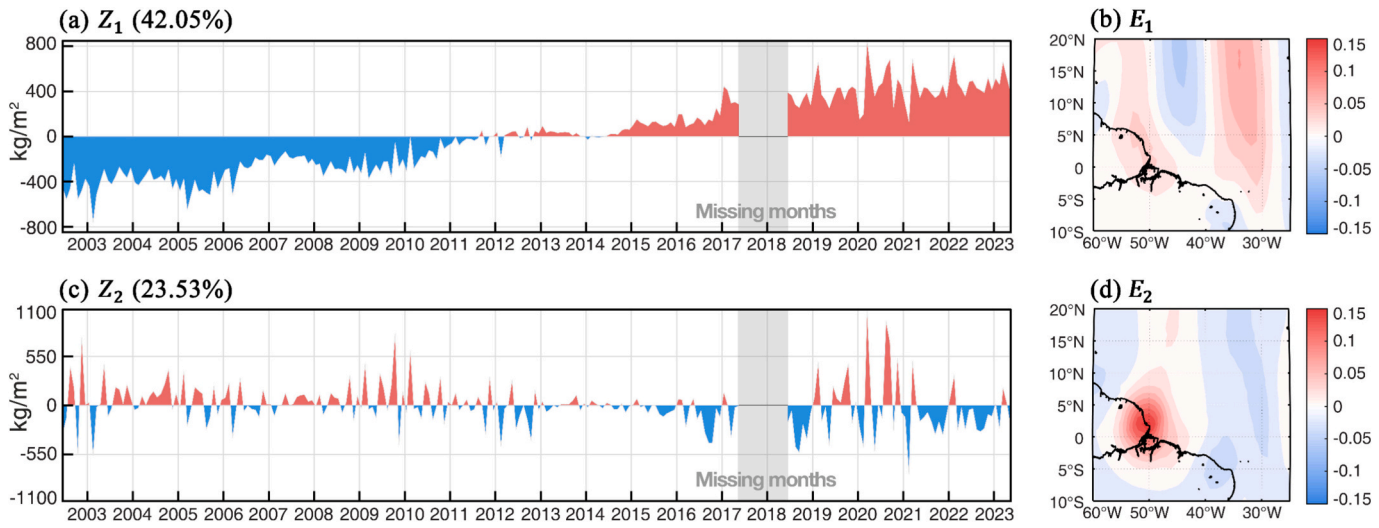

Fig. 5. EOF results for $\Delta X'$. (a) PC timeseries (Z_1) and (b) spatial pattern (E_1) of EOF mode 1. (c) PC timeseries (Z_2) and (d) spatial pattern (E_2) of EOF mode 2. The explained variance of each mode is provided in (a) and (c).

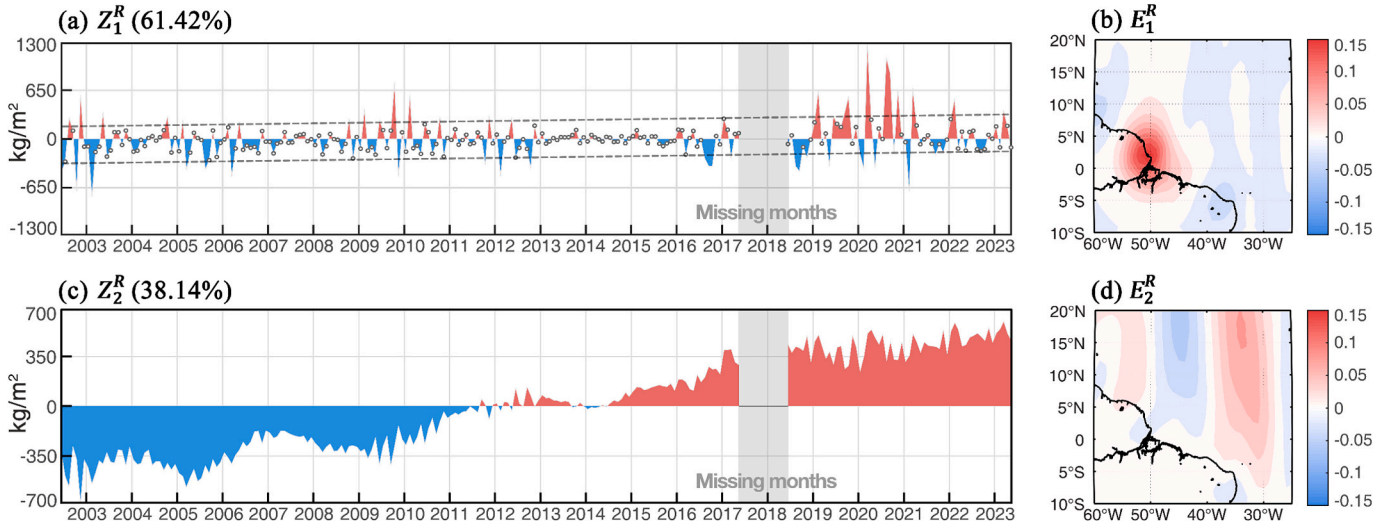

Fig. 6. REOF results for EOF modes 1 and 2 in Fig. 5. (a) PC timeseries (Z_1^R) and (b) spatial pattern (E_1^R) of REOF mode 1. (c) PC timeseries (Z_2^R) and (d) spatial pattern (E_2^R) of REOF mode 2. The explained variance of each mode is provided in (a) and (c). The 190 Gy circle points in (a) are sample data within the standard deviation (dashed lines) of the Z_1^R (trend).

$\Delta X''$ were rotated based on the VARIMAX criterion (see Eqs. (4) and (5) in Eom et al., 2017a, 2017b). The method adjusts the EOF spatial patterns to maximize variances at grid points, resulting in the new rotated frame. As a result, $\Delta X''$ can be represented as follows:

$$\Delta X''(x,t) = \sum_k E_k^R(x) Z_k^R(t) \tag{9}$$

where $E_k^R(x)$ is the k-th REOF spatial mode rotated from its original EOF mode. Because the VARIMAX method preserves the orthogonality of spatial modes during rotation, the corresponding PC time series, $Z_k^R(x)$, are simply given by projections of E_k^R on $\Delta X'$. After consecutively applying CSEOF and REOF analysis, the majority of variances associated with the anticipated ΔM_S signals are concentrated into one of the REOF modes. Then, we estimated the sediment accumulation rate of the Amazon River based on the ΔM_S-dominated REOF mode.

4. Results

4.1. CSEOF-REOF reconstruction

Using the CSEOF method in Eq. (4), we decomposed the residual GRACE/GFO signalΔX, which contains the Amazon sediment accumulation signals and various error contributions. Eigenvalues (λ_n) and their confidence limits ($\Delta\lambda_n$) of the CSEOF modes show that the first three modes are relatively well-separated, while the subsequent modes are not in this case (Fig. 4). The explained variances of the CSEOF modes from 1 to 3 are about 37.99 % (19.51 %, 9.55 %, and 8.94 %, respectively), and the monthly CSLVs (E_n^C) and the PC time series (Z_n^C) for them are shown in Supplementary section (Fig. S1, S2, and S3). These three modes exhibit apparent local pattern near the Amazon River mouth, possibly associated with sediment accumulation. Higher modes tend to lack expected patterns for sediment deposition with lower explained variance. Overall, the CSEOF approach appears to be able to separate noise (mode 4 and higher) from ΔX. We took modes 1, 2, and 3 to be signal modes for further analysis.

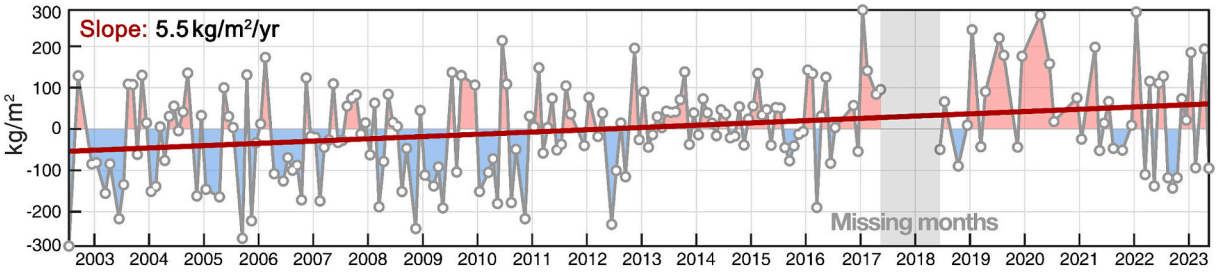

Fig. 7. Reduced PC timeseries of REOF mode 1 (Z_1^R) and its trend after removing outliers.

$\Delta X'$ is the sum of contributions of the first three CSEOF modes, but probably retains significant error contributions such as residual GRACE/GFO stripe noise. We applied conventional EOF decomposition to $\Delta X'$ and found the two leading EOF modes with significant explained variance contained signals with expected ΔM_S-behavior as in Fig. 5. Explained variances of modes 1 and 2 account for about 42.05 % and 23.53 %, respectively. For mode 2, the E_2 pattern (Fig. 5(d)) exhibits a relatively-well concentrated signal at the Amazon coast indicating that it contains much smaller noise contributions. Mode 1 is dominated by longitudinal stripe errors (Fig. 5(b)) with a large linear trend and interannual variability (Fig. 5(a)). Particularly in the E_1 pattern, we see a positive stripe at about 53°W longitude extending to the river mouth, probably indicating ΔM_S contribution to mode 1. Considering that the explained variance of EOF mode 1 is almost 2 times larger than mode 2, a ΔM_S contribution to mode 1 may be substantial.

The rotated spatial functions based on E_1 and E_2 indicate an enhanced signal separation in Fig. 6. There is increased explained variance of the rotated mode that (by its spatial pattern) is expected to be dominated by ΔM_S. The rotated spatial pattern E_1^R shows a clear circular-shape positive signal located at the Amazon River mouth. These REOF results suggest good signal separation of ΔM_S from error contributions in $\Delta X'$. Consequently, we take REOF mode 1 to be the contribution of ΔM_S due to Amazon sediment accumulation. In the presence of high-frequency noise, the time series associated with REOF mode 1 (i.e., Z_1^R) shows an apparent positive trend of 7.6 ± 4.7 kg/m^2/yr with a 95 % confidence interval (p = 0.004). The trend is likely biased from the noise, necessitating further suppression. We removed values from the time series that were larger than the standard deviation relative to the assumed positive trend (7.6 kg/m^2/yr). This procedure retained 190 out of the original 240 values as shown in Fig. 7. After suppressing the apparent outliers, the estimated trend was reduced to 5.5 ± 2.7 kg/m^2/yr. The expected sediment-related spatial pattern of E_1^R and the positive trend of Z_1^R are fully consistent with a steady mass increase near the Amazon river mouth.

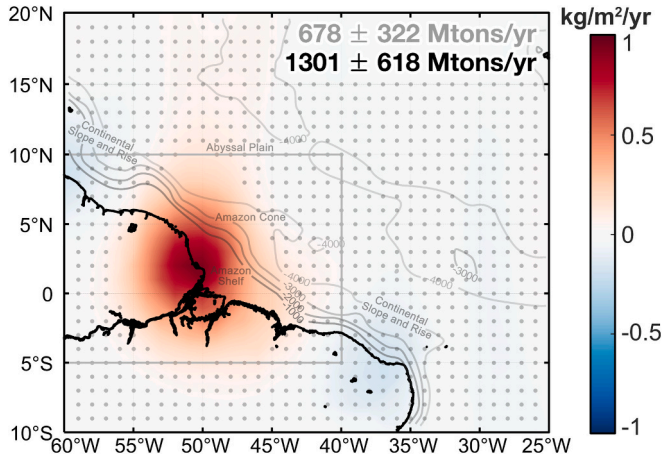

Fig. 8. Apparent annual mass accumulation rate at the Amazon coast. The gray dots represent areas below the noise level of 0.14 kg/m^2/yr. Areas without gray dots exceed this noise level, indicating that they contain sediment-related mass changes distinct from the background noise.

4.2. Sedimentary accumulation rate at the Amazon coast

Using REOF mode 1 spatial pattern (E_1^R) and the trend of 5.5 ± 2.7 kg/m^2/yr obtained from Z_1^R, surface mass change trends at grid points for June 2002 to May 2023 were estimated (Fig. 8). Most grid points except near the Amazon River mouth region have small values, probably associated with uncorrected error after the data reduction sequence. The Amazon coast and shelf area exhibit noticeable mass increase rates of approximately 1 kg/m^2/yr. Further, we see that the center of the mass increase in Fig. 8 is slightly skewed to the northwest from the river mouth, consistent with a predicted sedimentation area extending northwestward due to local current transport (Anthony et al., 2013; Molinas et al., 2020).

The mass fields across the entire region depicted in Fig. 8 can be aggregated to estimate the total sediment accumulation of the Amazon River. This approach is effective because the REOF analysis is designed to isolate sedimentation signals near the river mouth, while minimizing residual noise from other areas. Using this method, we obtain an estimate of 619 ± 294 Mtons/yr.

Alternatively, the total mass increase can be estimated by summing all smoothed signals within a few hundred kilometers of the source, including some land areas. To differentiate between signal and noise, we first estimated the standard deviation (1σ) of the background noise outside the regions outlined in the gray box, which is large enough to encompass the smoothed and attenuated sedimentation signals. Assuming a normal distribution for the noise, we defined values greater than 3σ (0.14 kg/m^2/yr) as sediment signals. The gray dots in Fig. 8 represent noisy grids. The total sedimentation signal from the grids, excluding the dotted regions, was calculated by multiplying the grid area (m^2) by the surface density (kg/m^2), yielding an estimate of 678 ± 322 Mtons/yr. We also applied the same procedure to estimate sediment accumulation in different study regions including the Amazon river outlet. Examples of these analyses are presented in Figs. S4-S6, which yield similar sedimentation estimates.

Fig. 8, however, illustrates the apparent sedimentation signal associated with the density contrast between sediment (~2500 kg/m^3) and seawater (~1000 kg/m^3) (Mouyen et al., 2018). Therefore, correcting for this density contrast is necessary to accurately determine the sedimentation signal. We multiplied the factor 1.6 (calculated as 2500/(2500–1000)) with the apparent estimate of 678 ± 322 Mtons/yr, resulting in a value of 1084 ± 515 Mtons/yr. This estimated total sedimentation rate of 1084 ± 515 Mtons/yr is likely still an underestimate of the actual value due to the limited spatial resolution of the GRACE/GFO data. The distribution shown in Fig. 8 represents a smoothed and attenuated version of the likely true sediment accumulation signal.

The impact of this underestimation is clearly illustrated through a synthetic test. In Fig. 9(a), we distributed appropriate mass values based on in-situ coring data from Kuehl et al. (1982), which report annual

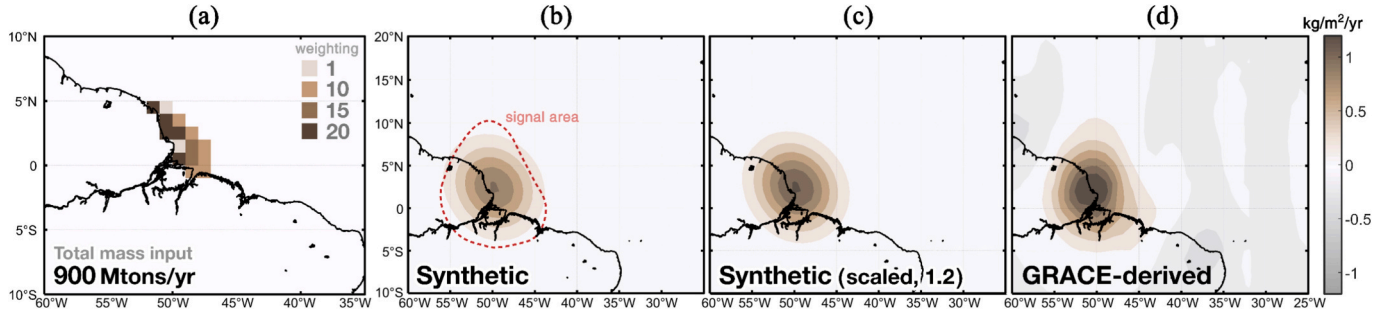

Fig. 9. Field-based synthetic test. (a) Mass distribution on the Amazon continental shelf. The total input mass of 900 Mtons/yr, weighted by 1, 10, 15 or 20 at grid points according to the accumulation rate (Fig. 8 in Kuehl et al., 1982). (b) 400 km Gaussian smoothing of (a), using the same colorbar as in (d). (c) Similar to (b) after applying a scale factor of 1.2 to (b). (d) The GRACE-derived accumulation rate of the Amazon sediments.

accumulation rates for the Amazon continental shelf, estimating sedimentation at 900 Mtons/yr. Fig. 9(b) displays the apparent mass distribution after applying a 400 km Gaussian smoothing to the grid values in Fig. 9(a). These smoothed mass fields exhibit a spatial pattern very similar to our results in Fig. 9(d) (which is analogous to Fig. 8 but uses a different colour scale, accounting for the density contrast between sediment and seawater), validating our estimate of sedimentation deposited by the Amazon River. The total sedimentation rate from the smoothed synthetic data in Fig. 9(b) for the same region selected for the sedimentation signal in Fig. 8 (indicated by the dotted red curve) is estimated to be about 767 Mtons/yr, lower than the original synthetic value of 900 Mtons/yr due to the smoothing effect. This underestimation can be corrected by applying a scaling factor (Landerer et al., 2012) of 1.2 (approximately 900/767) to the synthetic mass field in Fig. 9(a). Similarly, we applied the same scaling factor to the apparent sedimentation accumulation rate of 1084 ± 515 Mtons/yr, yielding a final annual sedimentation accumulation rate at the Amazon River mouth of 1301 ± 618 Mtons/yr.

4.3. Mass loss within the Amazon basin

Basin-scale hydrological mass changes from GRACE/GFO usually neglect mass loss due to continental weathering, erosion, and riverine sediment removal. The approach in this study provides a method to include this missing term in regional hydrological mass change estimates. Fig. 10(b) represents two different long-term trend estimates of the regional mass budget over the Amazon basin shown in Fig. 10(a). The gray line in Fig. 10(b) indicates a total mass trend estimated from leakage-corrected GRACE/GFO observations using the FM algorithm, showing a basin-scale trend of approximately 13.65 ± 6.15 Gtons/yr, reflecting both changes in total water storage and sedimentary mass changes over the basin. Adjusting this value using our estimate of sediment loss leads to a revised water mass change of about 14.95 ± 6.18 Gtons/yr (black), about 9.5 % larger than the observed value.

5. Discussion

Our estimate of 1301 Mtons/yr in the Amazon annual sedimentation is higher than previous estimates based on in-situ sedimentation coring, about 900 Mtons/yr (Kuehl et al., 1982). This difference can be attributed to uncertainties in both the coring data and satellite gravity observations, and may also stem from differing sampling periods. The accumulation rates at the coring points ranged from 0.1 to 2 cm/yr, so a typical 50 cm core contains sediments deposited over at least the last few decades and perhaps up to several centuries. However, Martinez et al. (2009) found suspended sediment discharge was approximately 688 Mtons/yr before 2001 but afterwards increased to 801 Mtons/yr. Inclusion of bed load would raise the total discharge rate beyond these figures. Our larger estimate is consistent with an increasing sediment accumulation rate which is not likely to be represented by in-situ coring estimates.

Residual stripe noise in reduced signals (ΔX) have contributions correlated with adjacent mass change signals, allowing effective separation by CSEOF decomposition. We conducted a test with synthetic data to show that the correlated nature of GRACE/GFO stripe noise was key to allowing separation of signal from noise. The synthetic data set included soil moisture from GLDAS (Global Land Data Assimilation System) (Rodell et al., 2004), FM-based GRACE/GFO values over Antarctica and Greenland, an Amazon River sedimentation signal of 1301 Mtons/yr, and spatially un-correlated synthetic noise. The synthetic noise consisted of normally-distributed random numbers, scaled to the GRACE/GFO SH degree spectrum. CSEOF decomposition did a poor job of separating signal from noise due to the lack of spatial and temporal correlation in the noise (Fig. S7). Thus, CSEOF analysis should be useful in other geophysical problems where small signals are to be separated from GRACE/GFO stripe noise.

We noted earlier that the Amazon sediment accumulation problem was well suited to GRACE/GFO analysis due to a lack of other major signals (earthquakes, GIA) which may be comparable in size to

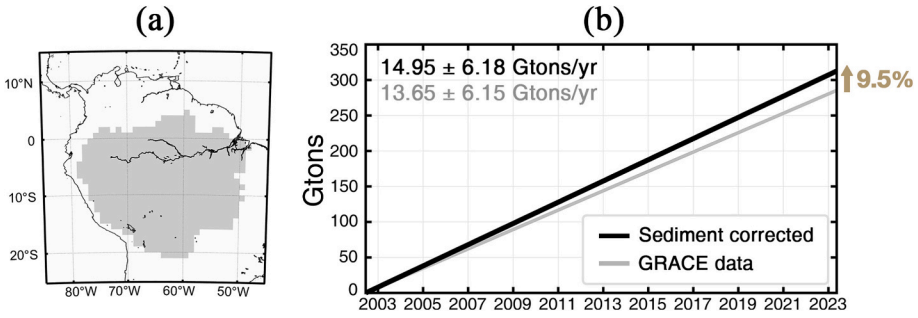

Fig. 10. Basin-scale mass trend over the Amazon basin with and without considering sediment discharge effect. (a) The domain of the Amazon basin. (b) Basin-scale mass trend from the leakage-corrected GRACE/GFO data (black) and the anticipated water-only contribution considering the mass loss effect inferred from the sediment discharge rate (gray).

sedimentation in terms of trend rates. So additional effort would be required to use GRACE/GFO to estimate depositional rates for other major rivers such as the Ganges-Brahmaputra and Yangtze (e.g., Han et al., 2006; Han et al., 2015; Jeon et al., 2023). The Amazon also offers a compact depositional region, whereas the Ganges-Brahmaputra Rivers (second largest sediment supplier in the world-Table 1) deposit only about half its sediments on the continental shelf with the other half carried into the Indian Ocean (Islam et al., 1999; Paszkowski et al., 2021).

Although gravity signals associated with sedimentation accumulation at other river margins are weak, it may become feasible to examine sediment accumulation rates for these rivers as satellite gravity missions extend with GFO and a future mission such as the Mass-Change and Geosciences International Constellation (MAGIC). The importance of extending the observational period is evident in Fig. S8. When the data period is reduced by half (10 years), the sedimentation trend is not significant, despite the spatial pattern distinctly highlighting the localized features along the river margin. Multi-decadal satellite gravity observations would provide insights into sedimentation processes in major river basins.

6. Conclusions

GRACE/GFO data have been used to estimate the long-term sediment accumulation rate at the Amazon River mouth. This has required first estimating water mass changes on both land and oceans from the GRACE/GFO data. After removing these we separated the residual into sedimentation and error signals via CSEOF and REOF methods leading to successful separation of the sedimentation signal localized along the Amazon coast. The total sediment accumulation rate was estimated to be 1301 ± 618 Mtons/yr, slightly larger than results from previous in-situ studies. This mass loss can be used to adjust the GRACE/GFO mass trend over the whole Amazon basin, which is usually interpreted as due to water alone. The sediment mass loss is about 9.5 % of the basin-scale total mass trend inferred from GRACE/GFO.

Our estimation methods employ techniques used routinely in geophysical studies, considering spatial leakage of signal, application of the sea level equation, and EOF analysis. The combination of these techniques shows that it is possible to estimate a relatively small sedimentation signal, and to identify the sedimentary contribution which accounts for 12.6 % of the regional GRACE/GFO mass trend near the river mouth. Careful attention to and application of similar processing methods should enable the estimation of new signals within GRACE/GFO data.

CRediT authorship contribution statement

Earthu H. Oh: Writing – original draft, Visualization, Formal analysis, Data curation, Conceptualization. **Ki-Weon Seo:** Writing – review & editing, Supervision, Methodology, Conceptualization. **Taehwan Jeon:** Writing – review & editing. **Jooyoung Eom:** Writing – review & editing. **Jianli Chen:** Writing – review & editing. **Clark R. Wilson:** Writing – review & editing.

Declaration of competing interest

The authors declare that they have no competing interests.

Acknowledgments

We appreciate Prof. Jusun Woo (of Seoul National University, South Korea) for his valuable advice on sedimentological interpretation. This research was supported by the National Research Foundation of Korea (NRF) grants (2022R1C1C2006586 & 2023R1A2C100489912) and the Korea Institute of Marine Science & Technology Promotion grant funded by the Ministry of Ocean Fisheries (RS-2023-00256677; PM24020). CRW was supported by NASA grants (80NSSC20K0820 & 80NSSC22K0906). JC was supported by the NSFC National Key Project (42394132) and Hong Kong RGC Collaborative Research Fund (C5013-23G).

Appendix A. Supplementary data

Supplementary data to this article can be found online at https://doi.org/10.1016/j.rse.2025.114688.

Data availability

The CSR RL06 GRACE datasets are distributed from GRACE Tellus website (https://grace.jpl.nasa.gov/data/get-data). Data analysis was conducted in MATLAB, with post-processing of GRACE/GFO data utilizing Free Software from Simons Laboratories (https://geoweb.princeton.edu/people/simons/software.html). Forward modeling and sea level filtering techniques followed those outlined by Chen et al. (2013), and CSEOF analysis was performed according to the computational procedures described by Kim and North (1997). Data displayed in this study can be shared on request to the corresponding author.

References

Aalto, R., Dunne, T., Guyot, J.L., 2006. Geomorphic controls on Andean denudation rates. J. Geol. 114, 85–99.
Alexander Jr., C.R., Nittrouer, C.A., DeMaster, D.J., 1986. High-resolution seismic stratigraphy and its sedimentological interpretation on the Amazon continental shelf. Cont. Shelf Res. 6, 337–357.
Anthony, E.J., Gardel, A., Proisy, C., Fromard, F., Gensac, E., Peron, C., Walcker, R., Lesourd, S., 2013. The role of fluvial sediment supply and river-mouth hydrology in the dynamics of the muddy, Amazon-dominated Amapá–Guianas coast, South America: a three-point research agenda. J. S. Am. Earth Sci. 44, 18–24.
Armijos, E., Crave, A., Espinoza, R., Fraizy, P., Santos, A.D., Sampaio, F., De Oliveira, E., Santini, W., Martinez, J.M., Autin, P., 2017. Measuring and modeling vertical gradients in suspended sediments in the Solimões/Amazon River. Hydrol. Process. 31, 654–667.
Biksham, G., Subramanian, V., 1988. Sediment transport of the Godavari River basin and its controlling factors. J. Hydrol. 101, 275–290.
Callede, J., Cochonneau, G., Alves, F.V., Guyot, J.-L., Guimaraes, V.S., De Oliveira, E., 2010. The river amazon water contribution to the Atlantic Ocean. J. Water Sci. 23, 247–273.
Chang, L., Tang, H., Yi, S., Sun, W., 2019. The trend and seasonal change of sediment in the East China Sea detected by GRACE. Geophys. Res. Lett. 46, 1250–1258.
Chen, J.L., Wilson, C.R., Tapley, B.D., Grand, S., 2007. GRACE detects coseismic and postseismic deformation from the Sumatra-Andaman earthquake. Geophys. Res. Lett. 34.
Chen, J., Wilson, C., Tapley, B., 2013. Contribution of ice sheet and mountain glacier melt to recent sea level rise. Nat. Geosci. 6, 549–552.
Chen, J., Cazenave, A., Dahle, C., Llovel, W., Panet, I., Pfeffer, J., Moreira, L., 2022. Applications and challenges of GRACE and GRACE follow-on satellite gravimetry. Surv. Geophys. 1–41.
Dai, A., Trenberth, K.E., 2002. Estimates of freshwater discharge from continents: latitudinal and seasonal variations. J. Hydrometeorol. 3, 660–687.
de Oliveira, P.A., Blanco, C.J.C., Mesquita, A.L.A., Lopes, D.F., Filho, M.D.C.F., 2021. Estimation of suspended sediment concentration in Guamá River in the Amazon region. Environ. Monit. Assess. 193, 79.
Eom, J., Seo, K.-W., Ryu, D., 2017a. Estimation of Amazon River discharge based on EOF analysis of GRACE gravity data. Remote Sens. Environ. 191, 55–66.
Eom, J., Seo, K.W., Lee, C.K., Wilson, C., 2017b. Correlated error reduction in GRACE data over Greenland using extended empirical orthogonal functions. J. Geophys. Res. Solid Earth 122, 5578–5590.
Farrell, W., Clark, J.A., 1976. On postglacial sea level. Geophys. J. Int. 46, 647–667.
Gardner, W.A., 1994. Cyclostationarity in Communications and Signal Processing. IEEE Press, New York.
Hamlington, B., Leben, R., Nerem, R., Han, W., Kim, K.Y., 2011. Reconstructing Sea level using cyclostationary empirical orthogonal functions. J. Geophys. Res. Oceans 116.
Han, S.C., Jekeli, C., Shum, C., 2004. Time-variable aliasing effects of ocean tides, atmosphere, and continental water mass on monthly mean GRACE gravity field. J. Geophys. Res. Solid Earth 109.
Han, S.-C., Shum, C.-K., Bevis, M., Ji, C., Kuo, C.-Y., 2006. Crustal dilatation observed by GRACE after the 2004 Sumatra-Andaman earthquake. Science 313, 658–662.
Han, S.C., Sauber, J., Pollitz, F., 2015. Coseismic compression/dilatation and viscoelastic uplift/subsidence following the 2012 Indian Ocean earthquakes quantified from satellite gravity observations. Geophys. Res. Lett. 42, 3764–3772.
Hannachi, A., Jolliffe, I.T., Stephenson, D.B., 2007. Empirical orthogonal functions and related techniques in atmospheric science: a review. Int. J. Climatol. 27, 1119–1152.

Islam, M.R., Begum, S.F., Yamaguchi, Y., Ogawa, K., 1999. The Ganges and Brahmaputra rivers in Bangladesh: basin denudation and sedimentation. Hydrol. Process. 13, 2907–2923.
Jeon, T., Seo, K.-W., Kim, B.-H., Kim, J.-S., Chen, J., Wilson, C.R., 2021. Sea level fingerprints and regional sea level change. Earth Planet. Sci. Lett. 567, 116985.
Jeon, T., Seo, K.-W., Han, S.-C., 2023. Impact of the solid Earth mass adjustment by the 2011 Tohoku–Oki earthquake on the regional sea level and hydrological mass change recovery from GRACE. Geophys. J. Int. 235, 1373–1383.
Kim, K.-Y., 2017. Cyclostationary EOF Analysis : Theory and Applications. Seoul National University Press.
Kim, K.-Y., North, G.R., 1997. EOFs of harmonizable cyclostationary processes. J. Atmos. Sci. 54, 2416–2427.
Kim, K.-Y., North, G.R., Huang, J., 1996. EOFs of one-dimensional cyclostationary time series: computations, examples, and stochastic modeling. J. Atmos. Sci. 53, 1007–1017.
Kim, K.-Y., Hamlington, B., Na, H., 2015. Theoretical foundation of cyclostationary EOF analysis for geophysical and climatic variables: concepts and examples. Earth Sci. Rev. 150, 201–218.
Kim, J.S., Seo, K.W., Jeon, T., Chen, J., Wilson, C.R., 2019. Missing hydrological contribution to sea level rise. Geophys. Res. Lett. 46, 12049–12055.
Kim, J., Na, H., Park, Y.-G., Kim, Y.H., 2020. Potential predictability of skipjack tuna (*Katsuwonus pelamis*) catches in the Western Central Pacific. Sci. Rep. 10, 3193.
Kuehl, S.A., Nittrouer, C.A., DeMaster, D.J., 1982. Modern sediment accumulation and strata formation on the Amazon continental shelf. Mar. Geol. 49, 279–300.
Landerer, Felix, W., 2012. Accuracy of scaled GRACE terrestrial water storage estimates. Water Resourc. Res. 48.4.
Loomis, B., Rachlin, K., Luthcke, S., 2019. Improved earth oblateness rate reveals increased ice sheet losses and mass-driven sea level rise. Geophys. Res. Lett. 46, 6910–6917.
Martinez, J.-M., Guyot, J.-L., Filizola, N., Sondag, F., 2009. Increase in suspended sediment discharge of the Amazon River assessed by monitoring network and satellite data. Catena 79, 257–264.
Meade, R.H., Dunne, T., Richey, J.E., Santos, U.D.M., Salati, E., 1985. Storage and remobilization of suspended sediment in the lower Amazon River of Brazil. Science 228, 488–490.
Meade, R.H., Yuzyk, T.R., Day, T.J., 1990. Movement and storage of sediment in rivers of the. United States and Canada.
Milliman, J.D., Meade, R.H., 1983. World-wide delivery of river sediment to the oceans. J. Geol. 91, 1–21.
Milliman, J.D., Syvitski, J.P., 1992. Geomorphic/tectonic control of sediment discharge to the ocean: the importance of small mountainous rivers. J. Geol. 100, 525–544.
Molinas, E., Carneiro, J.C., Vinzon, S., 2020. Internal tides as a major process in Amazon continental shelf fine sediment transport. Mar. Geol. 430, 106360.
Moquet, J.-S., Guyot, J.-L., Crave, A., Viers, J., Filizola, N., Martinez, J.-M., Oliveira, T.C., Sánchez, L.S.H., Lagane, C., Casimiro, W.S.L., 2016. Amazon river dissolved load: temporal dynamics and annual budget from the Andes to the ocean. Environ. Sci. Pollut. Res. 23, 11405–11429.
Mouyen, M., Longuevergne, L., Steer, P., Crave, A., Lemoine, J.-M., Save, H., Robin, C., 2018. Assessing modern river sediment discharge to the ocean using satellite gravimetry. Nat. Commun. 9, 3384.
Navarra, A., Simoncini, V., 2010. A Guide to Empirical Orthogonal Functions for Climate Data Analysis. Springer Science & Business Media.
Nittrouer, C.A., Kuehl, S.A., Sternberg, R.W., Figueiredo Jr., A.G., Faria, L.E., 1995. An introduction to the geological significance of sediment transport and accumulation on the Amazon continental shelf. Mar. Geol. 125, 177–192.
Nittrouer, C.A., DeMaster, D.J., Kuehl, S.A., Figueiredo Jr., A.G., Sternberg, R.W., Faria, L.E.C., Silveira, O.M., Allison, M.A., Kineke, G.C., Ogston, A.S., 2021. Amazon sediment transport and accumulation along the continuum of mixed fluvial and marine processes. Annu. Rev. Mar. Sci. 13, 501–536.
North, G.R., Bell, T.L., Cahalan, R.F., Moeng, F.J., 1982. Sampling errors in the estimation of empirical orthogonal functions. Mon. Weather Rev. 110, 699–706.
Paszkowski, A., Goodbred Jr., S., Borgomeo, E., Khan, M.S.A., Hall, J.W., 2021. Geomorphic change in the Ganges–Brahmaputra–Meghna delta. Nat. Rev. Earth Environ. 2, 763–780.
Peltier, W.R., Argus, D.F., & Drummond, R. (2018). Comment on "An assessment of the ICE-6G_C (VM5a) glacial isostatic adjustment model" by Purcell et al J. Geophys. Res. Solid Earth, 123, 2019–2028.
Richman, M.B., 1986. Rotation of principal components. J. Climatol. 6, 293–335.
Rodell, M., Houser, P., Jambor, U., Gottschalck, J., Mitchell, K., Meng, C.-J., Arsenault, K., Cosgrove, B., Radakovich, J., Bosilovich, M., 2004. The global land data assimilation system. Bull. Am. Meteorol. Soc. 85, 381–394.
Rudorff, C.M., Melack, J.M., Bates, P.D., 2014. Flooding dynamics on the lower Amazon floodplain: 1. Hydraulic controls on water elevation, inundation extent, and river-floodplain discharge. Water Resour. Res. 50, 619–634.
Shihora, L., Balidakis, K., Dill, R., Dahle, C., Ghobadi-Far, K., Bonin, J., Dobslaw, H., 2022. Non-tidal background modeling for satellite gravimetry based on operational ECWMF and ERA5 reanalysis data: AOD1B RL07. J. Geophys. Res. Solid Earth 127, e2022JB024360.
Simpson, M.R., Oltmann, R.N., 1993. Discharge-measurement system using an acoustic Doppler current profiler with applications to large rivers and estuaries. United States Geol. Survey Water-Supply Pap. 2395.
Swenson, S., Wahr, J., 2002. Methods for inferring regional surface-mass anomalies from gravity recovery and climate experiment (GRACE) measurements of time-variable gravity. J. Geophys. Res. Solid Earth 107, 2193.
Swenson, S., Wahr, J., 2006. Post-processing removal of correlated errors in GRACE data. Geophys. Res. Lett. 33, L08402.
Tapley, B.D., Watkins, M.M., Flechtner, F., Reigber, C., Bettadpur, S., Rodell, M., Sasgen, I., Famiglietti, J.S., Landerer, F.W., Chambers, D.P., 2019. Contributions of GRACE to understanding climate change. Nat. Clim. Chang. 9, 358–369.
Wahr, J., Molenaar, M., Bryan, F., 1998. Time variability of the Earth's gravity field: hydrological and oceanic effects and their possible detection using GRACE. J. Geophys. Res. Solid Earth 103, 30205–30229.
Wang, H., Yang, Z., Saito, Y., Liu, J.P., Sun, X., 2006. Interannual and seasonal variation of the Huanghe (Yellow River) water discharge over the past 50 years: Connections to impacts from ENSO events and dams. Glo. Planet. Chang. 50, 212–225.
Wang, H., Yang, Z., Saito, Y., Liu, J.P., Sun, X., Wang, Y., 2007. Stepwise decreases of the Huanghe (Yellow River) sediment load (1950–2005): impacts of climate change and human activities. Glob. Planet. Chang. 57, 331–354.
Wang, H., Saito, Y., Zhang, Y., Bi, N., Sun, X., Yang, Z., 2011. Recent changes of sediment flux to the western Pacific Ocean from major rivers in east and Southeast Asia. Earth Sci. Rev. 108, 80–100.